Sonocrystallization as an Efficient Way to Control the Size, Morphology, and Purity of Coordination Compound Microcrystallites: Application to a Single-Chain Magnet

Quentin Evrard, Felix Houard, Carole Daiguebonne, Guillaume Calvez, Yan Suffren, Olivier Guillou, Matteo Mannini, Kevin Bernot

Sonocrystallization as an efficient way to control size, morphology and purity of coordination compounds microcrystallites: application to a single-chain magnet

Quentin Evrard[1,2], *Félix Houard*[1], *Carole Daiguebonne*[1], *Guillaume Calvez*[1], *Yan Suffren*[1], *Olivier Guillou*[1], *Matteo Mannini*[3], *Kevin Bernot.*[1,4]*

1. Univ Rennes, INSA Rennes, CNRS, ISCR (Institut des Sciences Chimiques de Rennes), UMR 6226, F-35000 Rennes (France)

2. Current address: ARCNL (Advanced Research Center for Nanolithography), Science Park 106, 1098 XG Amsterdam (Netherlands)

3. LA.M.M. (Laboratory for Molecular Magnetism), Dipartimento di Chimica "Ugo Schiff" Università degli Studi di Firenze, INSTM, UdR Firenze Via della Lastruccia n. 3, Sesto Fiorentino (FI) 50019 (Italy)

4. Institut Universitaire de France (IUF), 1 rue Descartes, 75231 Paris, France

KEYWORDS: Sonocrystallization, Coordination compound, Purity control, Morphology control, Single-Chain Magnet.

GRAPHICAL ABSTRACT

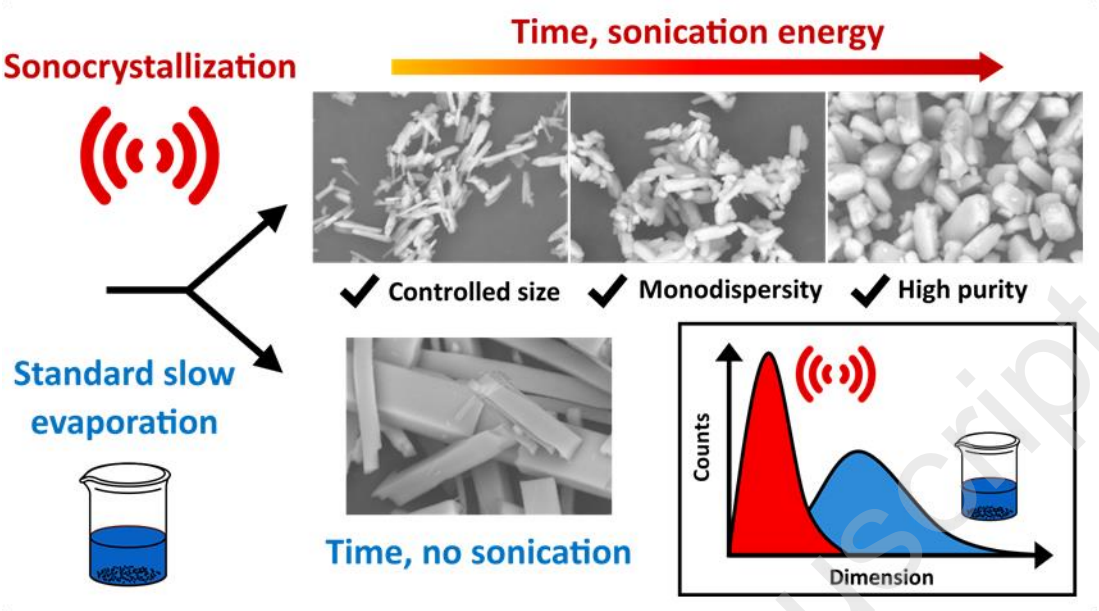

Sonocrystallization of a magnetic molecular material allows controlling the size, morphology and purity of its microcrystallites

ABSTRACT

Size, morphology and purity control of coordination compounds powders is a key stage for their conversion into materials and devices. In particular, surface science techniques require highly pure bulk materials with a narrow crystallite-size distribution together with straightforward, scalable and reproducible crystallization procedures. In this work we demonstrate how sonocrystallization, *i.e.* application of ultrasounds during the crystallization process, can afford, very quickly, powders made of crystallites with controlled size, morphology and purity. We show that this process drastically diminishes the crystallite-size distribution (low Polydispersity Indexes, PDI) and crystallite aspect ratio. By comparing sonicated samples with various silent crystallization conditions, we unambiguously show that the improvement of the crystallite morphologies and size-distribution is not due to any thermal effect but to the sonication of the crystallizing media. The application of sonocrystallization on crystallization batches of Single-Chain Magnets (SCM) maintains SCMs chemical integrity together with their original magnetic behavior. Moreover, luminescent measurements show that sonocrystallization induces an efficient micromixing that drastically enhances the purity of the SCMs powders. We thus propose that sonocrystallization, which is already used on organic or MOF compounds, can be applied to (magnetic) coordination compounds to readily afford bulk powders for characterization or shaping techniques that require pure, morphology- and crystallite-size-controlled powder samples.

INTRODUCTION

Ultrasonication provides energy to a liquid via acoustic cavitation.[1,2] Such phenomenon is due to the formation and collapse of bubbles caused by the expensive and compressive acoustic waves delivered to the liquid.[3] The chemist can use this energy i) to induce a chemical reaction between reactants: this is sonochemistry.[4] ii) to influence the crystal growth of a product: this is sonocrystallization.[5] This last is often associated with sonofragmentation[6] (crystallite breakage) and micromixing (mixing at the molecular scale).[7]

In first approximation, the collapse of cavitation bubbles has a thermodynamical and a mechanical effect on a reaction medium. First, the thermodynamic effect is related to the symmetric collapse of overgrown bubbles. This creates 'hot spots'[8] in the liquid that have very high local temperatures (≈ 5000 K) and pressures (≈ 1000 atm).[9] This collapse also generates very fast shockwaves (≈ 4000 $m.s^{-1}$) and high pressure amplitudes (≈ 10^6 kPa).[10] Such unusual and local reaction conditions can induce chemical reactions that are not accessible by standard means. This is the main driving force of sonochemical reactions.[4,8]

Second, the mechanical effect is due to the asymmetric collapse of cavitation bubbles close to the surface of a crystal. This generates a high-speed liquid stream[11] with velocities superior to 100 $m.s^{-1}$. This phenomenon can be used for example to fragment aspirin,[12] to break ultra-thin Ge nanowires,[13] to disperse TiO_2 agglomerates,[14] to roughen the surface of spherical Zn particles[15] or to partially melt metallic particle.[16] This mechanical effect is thus the main driving force of sonofragmentation.[6]

When a reaction media is sonicated, it is hard to disentangle the sonochemical and the subsequent sonocrystallization processes. For the latter, it is generally accepted that it occurs at a timescale when the chemical reaction is already performed Accordingly, the first report of sonocrystallization, by Richards and Loomis in 1927,[17] highlights that it reduces the

induction time,[9] that is the time elapsed between supersaturation and the appearance of crystals.[18] It is now known that this time is linked with the presence of a Metastable Zone Width (MZW) which is the zone where supersaturation occurs right before the crystallization. By consequence, sonocrystallization avoids secondary crystallization and agglomeration[19] that create high particle-size distribution.

The underlying mechanisms of sonocrystallization and its use on the different stages of the crystallization process have been reviewed recently.[20,21] Ultrasounds are used at the industrial scale[22] mainly on pharmaceutical[23-27] or food compounds[28,29] to control crystal shape, size distribution and morphology.[6,9,19,30] Sonocrystallization increases the reproducibility of the crystal growth process.[20,31] Many small molecules can be processed by ultrasonication such as NaCl,[32] polymorphs of lactose[33] or paracetamol.[25-27] For example, the ultrasonic processing of paracetamol solution during crystal growth produces powders with enhanced mechanical behavior that allow easy compaction into tablets without requiring any excipients.[26] It is also possible to use sonocrystallization to synthesize more elaborated molecules such as Mn(II) precursor for manganese oxide[34] or extended coordination networks such as metal-organic coordination polymers.[35] However, to the best of our knowledge sonocrystallization has not been used on coordination material targeted for their magnetic properties.

Magnetic coordination polymers[36-38] are extended molecular networks[39,40] that display interesting magnetic properties such as magneto-caloric effect,[41] nanoporous magnetism,[42] or single-chain magnet behavior.[43-59] These compounds face drawbacks as far as their conversion into materials is targeted. Indeed, they are insoluble by nature and their purification by standard techniques can be tricky. It can be found surprising but in most reports, magnetic investigations are still performed on samples made of hand-picked crystal from a mother solution. This is an issue as magnetic coordination polymers are made of

several building blocks (magnetic and/or non-magnetic) assembled by chemical reaction and thus unreacted species can act as magnetic impurities that will severely degrade the overall magnetic behavior. If neutral building blocks are used, local stoichiometry changes can induce crystallization of several undesired phases because reactant ratios are not driven by electroneutrality. Obviously, these polyphasic and/or impure samples are not suitable for surface deposition because local and global magnetic properties can be totally different.

In this work, we use a well-known mono-dimensional magnetic coordination polymer of formula $[Tb(hfac)_3(NIT\text{-}PhOPh)]_n$ (where $hfac^-$ = hexafluoroacetylacetonate and NIT-PhOPh = 2,4'-benzoxo-4,4,5,5-tetramethylimidazoline-1-oxyl-3-oxide nitronyl nitroxide radical) (Figure 1).[60] This compound behaves as a Single-Chain Magnet (SCM) and is a target compound for the design of molecule-based magnetic data storage devices. Indeed, when compared to zero-dimensional compound such as Single-Molecule Magnets[61] (SMMs), SCMs are not sensitive to parasites magnetic relaxations (Raman, quantum tunneling of the magnetization…) that cancel the magnetic information encrypted on the molecules. However, the deposition of SCM on surface to make devices is a huge challenge because the transfer of polymeric chains on surfaces is particularly tricky.[62] The first step toward this goal is to obtain SCM powders suitable for dispersion and deposition via wet deposition techniques.[63,64] This requires pure and, most of all, homogenous powders with a narrow crystallite-size distribution and a straightforward, scalable and reproducible crystallization procedure. In this work we demonstrate how sonocrystallization is a useful tool to achieve these goals.

EXPERIMENTAL SECTION

Synthesis

Syntheses of $[Tb(hfac)_3(NIT\text{-}PhOPh)]_n$ (Figure 1) have been optimized from the previously reported procedure.[60] 1.3 mmol (106.1 mg) of $[Tb(hfac)_3{\cdot}2H_2O]$ is dissolved in

40 mL of boiling heptane (T_b= 98 °C) and concentrated to 12 mL. 1 mmol (32.5 mg) of NIT-PhOPh is then added to the boiling solution along with 3 mL of $CHCl_3$ (T_b= 61 °C). The process is thus performed in anti-solvent conditions with $CHCl_3$ as solvent and heptane as anti-solvent. The obtained deep blue solution is then directly transferred in a 20 mL vial for immediate sonication (Figure 2 and 3).

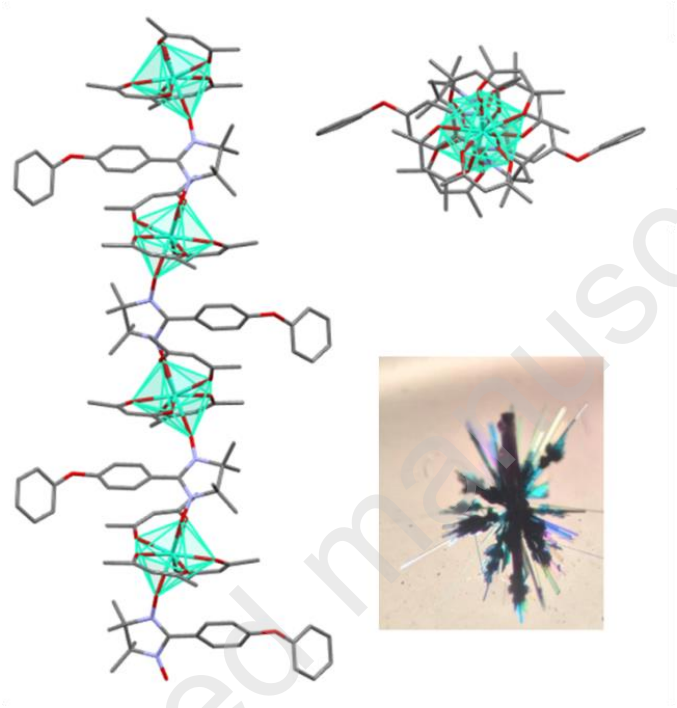

Figure 1. Representation of $[Tb(hfac)_3(NIT\text{-}PhOPh)]_n$ (redrawn from[60]) along (right) and perpendicular (top left) to the chain. Bottom right: picture of a cluster of single-crystals suitable for crystal structure determination.

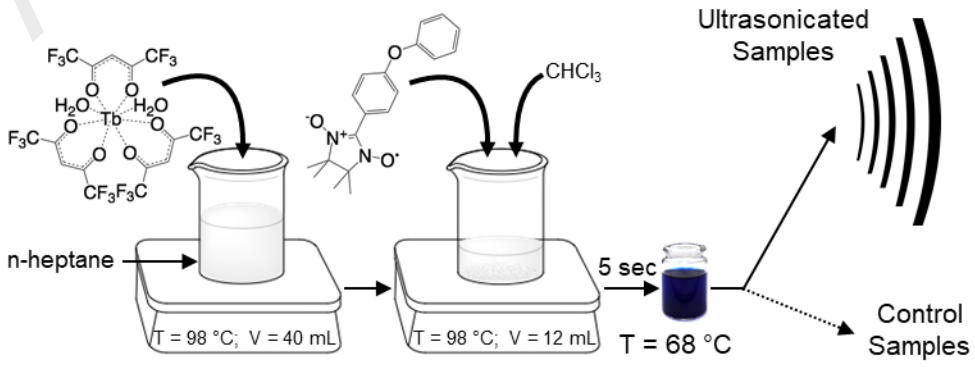

Figure 2. Schematic representation of the crystallization and synthesis procedures.

Sonication procedures

Sonication is performed with a Hielscher UP400St sonicator using a S24d3 sonotrode operating at a fixed frequency (24kHz). The temperature of the solutions is continuously monitored during the crystallization process. The respective positions of the sonicating horn, the temperature sensor, and the vial are carefully checked to ensure good reproducibility. All the experiments are performed in identical 20 mL crystallization vials. Right after the transfer of the solution into these vials, six different procedures are followed (Figure 4):

i) Three samples have been prepared to observe the influence of the sonication on the crystallization process. In our case we used pulsed-sonication. This technique allows delivering a high amount of energy to the solution during a high amount of time without boiling of the solvent because of ultrasound-induced heating (Figure 3, Figures S1-S2). We have chosen a 90% pulse rate (cycles of 0.9 s of sonication and 0.1 s of silence) that corresponds to an energy delivery of $\approx$ 24 J per pulse. This energy delivery induces a temperature plateau at 56°C (Figures 4 et S2) that is an ideal temperature because it corresponds to the temperature where early signs of crystallization are observed in silent conditions (observation via Tyndall effect). This also corresponds to a critical concentration for crystallization of 1.7 mmol.L^{-1} (Figure 3). Three ultrasonicated samples are tested and are named UltraSonicated 1 (US1), US2 and US3. The total amount of energy received by the solution is approximately 75, 150 and 300 kJ that corresponds to sonication times of 52, 100 and 193 min, respectively (Figure 4).

ii) Three control samples have been prepared to observe the crystallization reaction under silent conditions. Crystallization time is tested on two solutions that are let cool down after transfer in the vial and filtered after 5 minutes ('Short' crystallization, sample S) or 24 hours

('Long' crystallization, sample L). The sample L is the usual crystallization procedure that provides coordination compounds in their crystalline form.[60] Thermal effect is tested on a sample that is thermalized for 100 min at 56°C. These conditions mimic the temperature plateau generated by the sonication of sample US2 (Figure S3). This sample is named sample T for 'Thermally-assisted crystallization conditions'. This control sample allows discriminating thermal and ultrasound effect on the crystallization.

Last, all solutions (except sample L) have been hot-filtered to avoid secondary recrystallization in the fritted funnel.

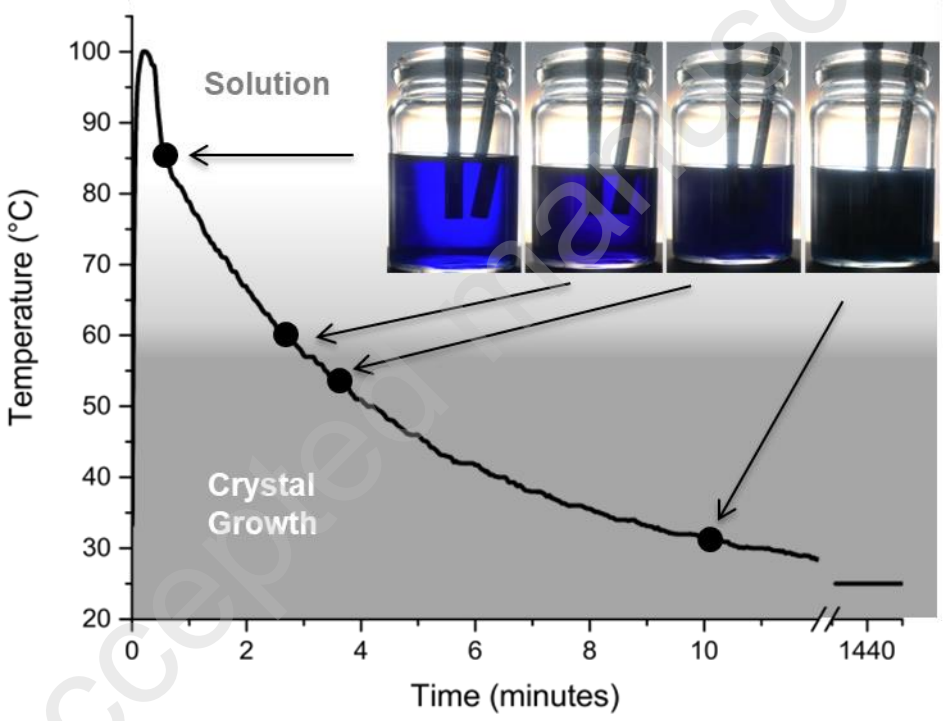

Figure 3. Experimental temperature profile measured during the crystallization of sample L (24 h crystallization under silent conditions) with several pictures of the crystallization vials during the first minutes of cooling (in inset). The two rods are the sonotrode and the thermometric probe. Turbidity is observed below 56°C for an estimated critical concentration of 1.7 mmol.L^{-1} (see text).

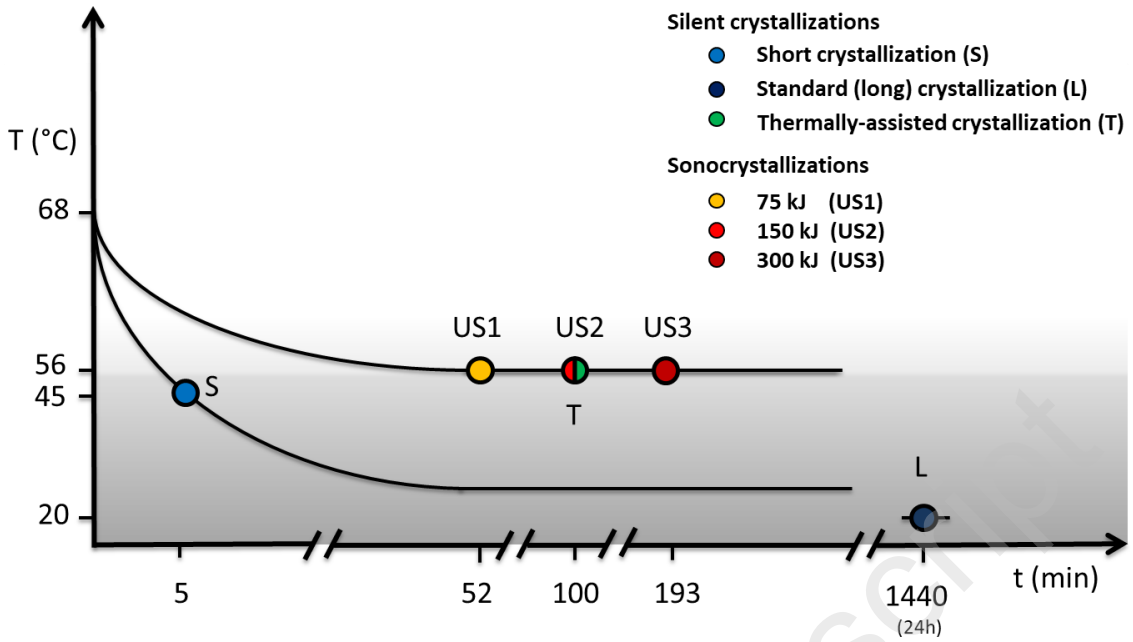

Figure 4. Schematic representation of the thermal profiles for samples US1, US2, US3 (sonocrystallized with approximately 75, 150 and 300 kJ of energy delivery by sonication), S, L and T (control samples of Short, Long, and Thermally assisted crystallization, respectively).

Powder X-Ray diffraction.

Experimental diffraction patterns have been measured with a Panalytical X'pert Pro diffractometer equipped with a PIX'Cel detector. Spectra were collected using a CuKα (45 kV, 40 mA, $\lambda = 1.542$ Å) in a θ/θ configuration. Calculated pattern is generated using the Mercury program (Version 3.9 RC1) from CCDC on the basis of the deposited cif file.[65]

FT-IR measurements.

FT-IR spectra were collected using a Perkin Elmer Frontier UATR spectrometer directly on the powders with a measurement range from 4000 to 550 cm^{-1} and a resolution of 1 cm^{-1}.

SEM measurements.

SEM images were obtained using a Hitachi Tabletop TM-1000 microscope (version 02.11 (Hitachi High-Technologies, Corporation Tokyo Japan)) equipped with a silicon drift detector with an energy resolution of 165 eV. Samples were observed with an acceleration voltage of 15 kV under high vacuum. The samples were put on carbon disc, immobilized with double sided carbon tape and measured with an angle of 22° from the beam. SEM pictures have been taken with magnification of x1000 (sample S and L) and x5000 (US1, US2, US3, T).

Size distribution analysis.

The SEM images have been analyzed using the Gwyddion software (version 2.50).[66] For each sample, 400 crystals have been measured (length and width). On each sample the mean length and mean width are calculated together with the standard deviation (σ) and the Polydispersity Index (PDI = σ^2 / mean value).

It can be noted that IUPAC recommended in 2009 that 'dispersity' (symbolized 'Đ'), replaced PDI.[67] This terminology has been progressively adopted by the polymer science community because Đ can be simply calculated as $Đ = M_w/M_n$ with M_w the mass-average molar mass and M_n the number-average molar mass. Similarly the 'polydisperse' and 'monodisperse' terminologies have been changed for 'uniform' and 'non-uniform'. However, as far as particle counting is concerned the PDI terminology is still the one that is commonly used, in particular in the Dynamic Light Scattering (DLS) community.[68-70] PDI is a simple way to characterize the dispersion of a given value (length, width, diameter,…) over a particles population. It takes values from 0 (perfectly monodisperse (uniform) sample) to 1 (perfectly polydisperse (non-uniform) sample). The commonly accepted limit for monodispersity is PDI < 0.3 (drug delivery applications for example)[71] while PDI > 0.7 is considered extremely polydisperse.[68] As our particles are needle-shaped we provide PDI values for length (PDI_l) and width (PDI_w) (Figure 5, Table 1).

Luminescence measurements

Luminescence emission spectra were measured with a Horiba Jobin-Yvon Fluorolog-III fluorescence spectrometer equipped with a 450 W Xe lamp. The luminescence was collected with a Hamamatsu R928 UV–vis photomultiplier in the 190–860 nm range. All samples were measured in the same slit configuration to allow easy comparison: the emission was measured directly on quartz cuvette containing the powder (in reflection mode at 90°) with a step of 1 nm, an excitation of 312 nm with 8 nm slits and a grating of 1200 grooves/mm. Appropriate filters were used to remove residual lamp excitation, scattered light and associated harmonics, the spectra were reference corrected for the excitation source intensity variation and the emission spectral response of the detector.

Magnetic measurements

Static (dc) magnetic measurements were performed with a Quantum Design MPMS SQUID magnetometer equipped with a Reciprocating Sample Option (RSO) sample holder. All the samples have been measured on microcrystalline powder pressed into pellets and wrapped with Teflon to avoid in-field orientation of the crystallites. Measurements were corrected from the contribution of the sample holder and diamagnetic corrections were calculated via Pascal's constants.[72]

RESULTS AND DISCUSSIONS

Silent crystallization procedures have been performed for 5 min (sample S, short and silent crystallization) and 24 h (sample L, the usual long and silent crystallization).[60] As expected, they afford very different SEM images (Figure 5). Sample S is made of very thin needles with an average width and length of 0.34 µm and 2.62 µm, respectively (aspect ratio, *i.e.* ratio between crystallite length and width, of 7.71). As the crystallization time is

increased (sample L) the mean width increases more than ten folds (3.82 µm) and the mean length reaches 12.83 µm (aspect ratio of 3.36).

On sample S, high PDI values are observed (PDI_w = 0.38 and PDI_l = 0.83, Table 1) as a consequence of an uncontrolled crystallization made of primary and secondary crystallization germs. If these small crystallites are let grown over 24 h as in sample L, the size distribution becomes so large that σ does not describe the distribution properly and very high (PDI_w = 0.92) or senseless (PDI_l > 1) are found. These two samples show that usual crystallization procedures don't provide batches with homogenous crystallite dimensions and small crystallites can be mixed with almost 20 times bigger ones. The very high polydispersities observed are a drawback for homogenous and simultaneous solubilization of the crystallites for surface sciences purposes. SEM image of sample L, illustrates another main issue of the standard crystallization procedure as impurities that stand as white spots on crystallites can be observed easily (see luminescence measurement section for their characterization).

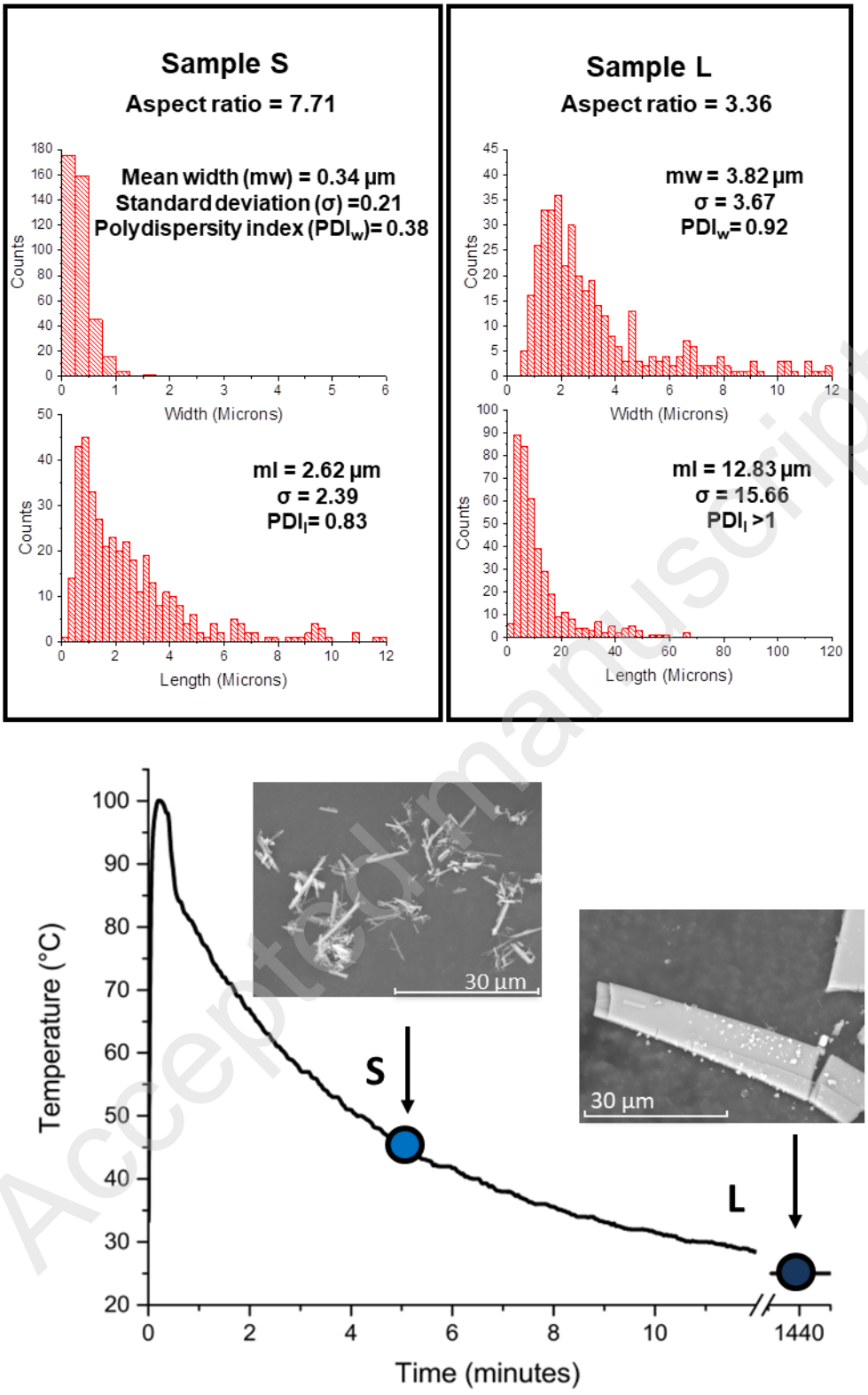

Figure 5. Experimental thermal profile (bottom), example of SEM images (x1000, in inset), and particle counting (top) for sample S (short crystallization, 5 minutes) and sample L (standard (long) crystallization procedure of 24 h) obtained in silent conditions. Note that the

histograms scales for the width and length of L are multiplied by 2 and 10, respectively. Abbreviations: mw = mean width, ml = mean length, σ = standard deviation, $PDI_{w,l}$ = Polydispersity Indexes in width or length. PDI_l for sample L is not representative (see text).

Sonocrystalization for morphology and size distribution control of SCM microcrystallites.

Three different samples (US1-US3) have been sonocrystallized by varying the sonication time and thus the energy delivery in the crystallization vials. SEM images show that the crystallite mean lengths are in the range 2.63 - 4.25 µm (Figure 6) to be compared with 2.62 µm for sample S and 12.83 µm for L. This highlights that the sonication prevents the growth of the needles along their longitudinal axis and tends to provide crystals with more isotropic shapes. The more the sample is sonicated, the bigger the crystals are and the less the needle shape is pronounced. Aspect ratios are 4.05, 2.91 and 2.07 for US1, US2 and US3, respectively.

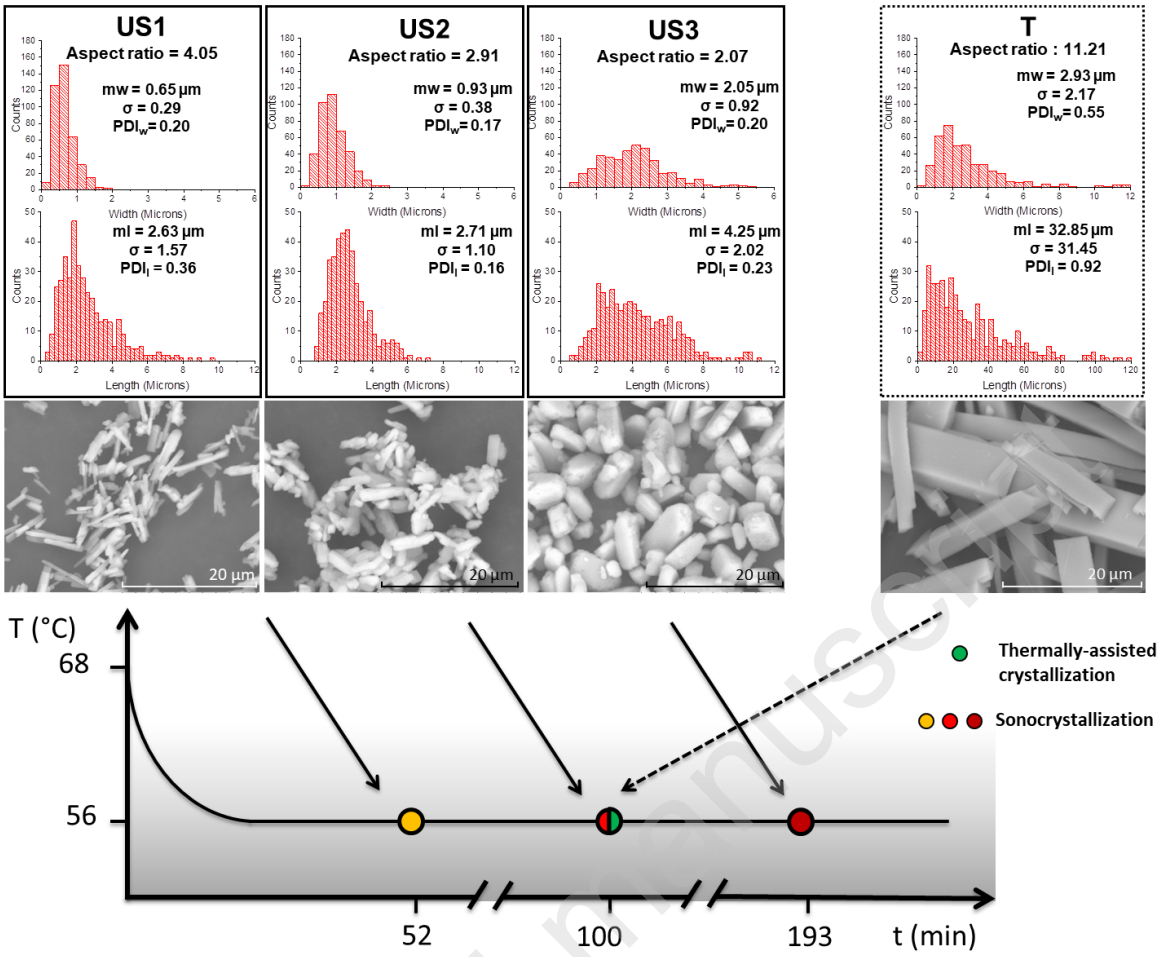

Figure 6. (for double column). Schematic thermal profile (bottom), examples of SEM images (x5000 magnification, in inset) and particle counting (top) for sample US1 (pulse-sonicated for a total energy delivery of approximately 75 kJ), US2 (150 kJ), US3 (300 kJ) and the control sample T (silent conditions and thermalized at 56°C for the same duration as US2). Note that the histograms scale for the width and length of T are multiplied by 2 and 10, respectively. Abbreviations: mw = mean width, ml = mean length, σ = standard deviation, $PDI_{w,l}$ = Polydispersity Indexes in width or length.

Additionally, as the sonication proceeds the crystal edges are rounded because the sonication shockwave and the asymmetric collapse of cavitation bubbles induce mechanical damages on the crystal region that have the least mechanical robustness. This is particularly noticeable on US3, that is the most sonicated sample. One of the most spectacular effects of the sonication

is its influence on particle-size distribution. All sonicated samples have very low PDI values when compared with S and L (Table 1). A clear trend is observed from S (PDI_w = 0.38, PDI_l = 0.83), to US1 (0.20, 0.36) and US2 (0.17, 0.16). It is interesting to note that US3 have small PDI values (0.20, 0.23) but it does not follow this trend. At this stage, we don't have definitive explanations. However, it can be hypothesized that the larger distribution in crystallites lengths is linked with crystal sizes that are big enough to be comparable with the ones of the cavitation bubbles (maximal size of 10 µm in our operating conditions).[73,74] So the longer crystallites break, increasing the length distribution. Accordingly, as far as homogenous crystallite-size is targeted, the US2 sample is the most optimized one: it has the lowest PDI values, and the more Gaussian-shaped repartition of the population of crystallite dimension.

As detailed in experimental section the sonication conditions generate a thermal plateau at 56°C. Obviously this could be the reason for a so strong difference in aspect ratio along the S, L, US1-US3 series (Figure 6 and Table 1). In order to rule-out any purely thermal effect on the crystal growth, a control sample that mimics the thermal profile of US2 (Figure S3) has been prepared by conventional heating and is hereafter called sample T for 'Thermally-assisted crystallization' (see experimental section). SEM image shows that T is drastically different from US2 (Figure 6). The thermal plateau and the absence of sonication produced very big crystallites with mean width and mean length that are 3 and 12 times bigger, respectively than that of US2. Notably the mean length is in an extremely large range (5 - 155 µm). This induces the highest aspect ratio of all 6 samples (11.21) but also very high Polydispersity Indexes with PDI_w = 0.55 and PDI_l = 0.92. In the absence of sonic shockwaves crystal edges and apexes are very sharp. Additionnaly the comparison of T with L shows, as expected, that crystallization with a temperature plateau at the highest temperature efficient

for crystal growth (56°C here) is favorable over cooling toward room temperature to provide big crystallites (longest crystal in L is only 65 µm long).

Table 1. Main morphologic parameters gathered from the SEM images of the six samples*

		Width			Length			Aspect ratio
		Mean width (µm)	σ	PDI_w	Mean lenght (µm)	σ	PDI_l	
Control samples	**Short crystallization (S)**	0.34	0.21	0.38	2.62	2.39	0.83	7.71
	Thermal crystallization (T)	2.93	2.17	0.55	32.85	31.45	0.92	11.21
	Standard (long) crystallization (L)	3.82	3.67	0.92	12.83	15.66	**	3.36
Ultrasonicated samples	**US1**	0.65	0.29	0.20	2.63	1.57	0.36	4.05
	US2	0.93	0.38	0.17	2.71	1.10	0.16	2.91
	US3	2.05	0.92	0.20	4.25	2.02	0.23	2.07

Abbreviations σ = standard deviation, $PDI_{w,l}$ = Polydispersity Indexes in width or length.

*All values calculated on 400 crystallites per sample (see experimental section).

** PDI > 1 (see experimental section).

Table 1 shows that sonocrystallization of $[Tb(hfac)_3(NIT\text{-}PhOPh)]_n$ provides more isotropic crystallites (small aspect ratios) than standard crystallization as already seen on some organic compounds.[75-77] Similarly, particle-size distribution becomes considerably smaller upon sonication[78,79] and the most optimized sonicated sample is US2 ($PDI_{w,l}$ = 0.17,0.16 on). Interestingly, sonication is efficient in optimizing the PDI as long as crystal-size remains below cavitation bubbles dimension (limiting case of US3).

Overall, the more the crystals are sonicated the bigger they are. This is in agreement with some previous reports[6,7] but the reason for this counterintuitive finding is still debated: a recent and very documented review stated that *"no consensus can be found in literature on*

the effect on ultrasound on the growth rate".[20] Several hypotheses can be formulated to explain the observed crystal growth under sonication:

i) a balance between a positive ultrasound effect on nucleation (sonocrystallization) and a negative ultrasound effect on crystal growth (sonofragmentation).[20,80] More precisely, bubbles cavity can acts as nucleus for primary heterogeneous nucleation[20,81] but as the bubbles explode they can fragment first nuclei[82,83] and creates a large amount of smaller secondary nucleating sites. This dual contribution is particularly likely to occur in our system because our 24 kHz ultrasound frequency corresponds to a frequency domain in which cavitation bubbles can be both in a transient or stable mode and lead to nucleation or fragmentation.[3,7,22,31,80] US2 is thus the most optimized sample on the crystal growth point of view.

ii) an enhanced micromixing in the solution[32,79,84] where sonication induces a more homogenous anti solvent and temperature distribution in the vial than in standard condition. Van Gerven *et al*,[7] detail that ultrasonication enhances micromixing in three ways: first, implosion of transient cavitation bubbles causes turbulences in the reaction media. Second, stable cavitation bubbles induce convection in their surroundings. Third, dissipation of ultrasound energy induce vortices in the reaction medium. In any case, efficient micromixing induces a more homogenous anti-solvent and temperature distribution in the vial than in standard condition. This induces more homogenous local crystal growth condition for every nucleation point and provides overall a smaller crystal-size distribution. In any case, the crystal growth observed under sonication is not a purely thermal effect as shown by the comparison of US2 with T sample.

Sonocrystallization for purity control of SCM microcrystallites.

The synthesis of $[Tb(hfac)_3(NIT\text{-}PhOPh)]_n$ can afford many different impurities such as unreacted $[Tb(hfac)_3 \cdot 2H_2O]$ complex or NIT-PhOPh radical as well as undesired phases of non-polymeric molecules of formula $(Tb(hfac)_3)(NIT\text{-}PhOPh)_2$ [85] (Figure 7). This is a direct consequence of the use of neutral building blocks as reactant because the formation of the final product is driven by local stoichiometry and not by product's electroneutrality. The purity control of $[Tb(hfac)_3(NIT\text{-}PhOPh)]_n$ sample is thus a significant issue.

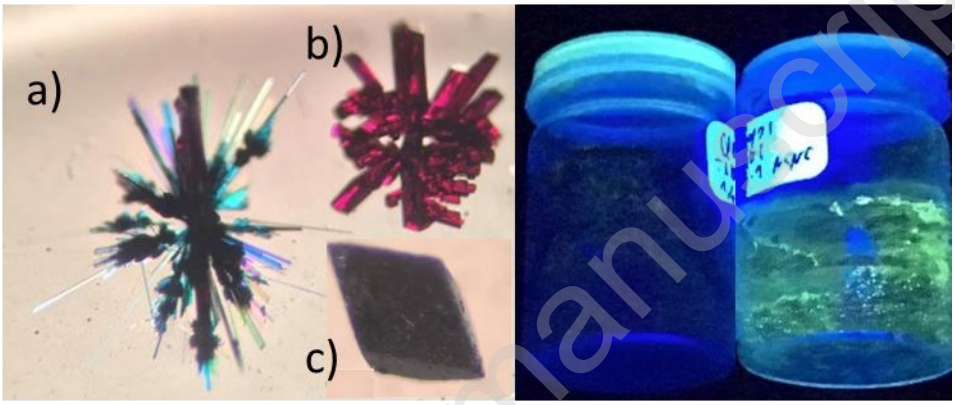

Figure 7. Examples of the various crystallites that can be found in a crystallization batch of $[Tb(hfac)_3(NIT\text{-}PhOPh)]_n$ (left); the targeted chains produces blue-green needles (a) but two phases of non polymeric compound of formula $(Tb(hfac)_3)(NIT\text{-}PhOPh)_2$ can be found. (b and c). Vials with and without unreacted luminescent $[Tb(hfac)_3 \cdot 2H_2O]$ (right).

All samples have been comparatively analyzed by Infra-Red (IR) spectroscopy, Powder X-ray Diffraction (PXRD) and solid-state luminescence measurements (Figure 8). IR spectra of all samples are superimposable and show that sonication preserves the chemical integrity of $[Tb(hfac)_3(NIT\text{-}PhOPh)]_n$ (2954 cm^{-1} and 2871 cm^{-1} ν(C-H), 1650 cm^{-1} ν(C=C), 1610 cm^{-1} $\nu(C{=}C_{arom})$, 1560 cm^{-1}, 1533 cm^{-1} and 1501 cm^{-1} ν(C=C), 1334 cm^{-1} ν(NO), 1298 cm^{-1} ν(CO)). Similarly PXRD patterns show that all samples match the simulated

diffractogram obtained from crystal structure data (CCDC N°262704), showing that sonication does not induce any structural changes between the samples.

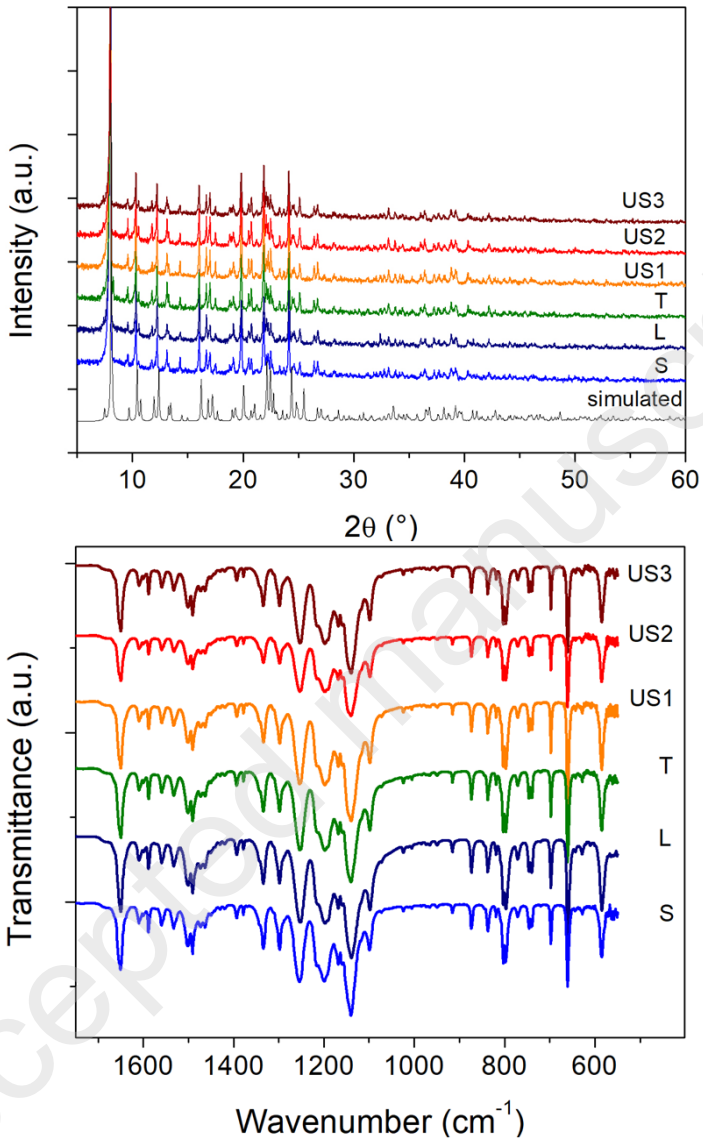

Figure 8. Comparison of X-ray powder diffractograms (top) and infrared spectra (bottom) of the six samples (S, L, T, US1 – US3) of $[Tb(hfac)_3(NIT\text{-}PhOPh)]_n$.

If infrared spectroscopy and PXRD are efficient techniques to check the chemical and structural integrity of $[Tb(hfac)_3(NIT\text{-}PhOPh)]_n$, they are not sensitive enough to detect traces of amorphous impurities. Moreover, highly sensitive characterizations such as elemental

analysis are not always accurate[86] on coordination polymers because they can host crystallization solvent. We have recently demonstrated that solid-state luminescence measurement can be used to verify the purity of coordination polymers made of emissive building blocks.[87] This is the case of $[Tb(hfac)_3(NIT\text{-}PhOPh)]_n$that is obtained by reacting: i) $[Tb(hfac)_3{\cdot}2H_2O]$[88] that shows a green and line-shaped emission that is characteristic of Tb^{III} ion.[89,90] It is so luminescent that we have shown that it can be detected on surface at the molecular scale by standard luminescent setups[88] ii) nitronyl-nitroxide radicals, that show broad near-IR emission[91] that can be blue-shifted[92] or cancelled upon metal ion coordination.

This sensitivity to minute amount of uncoordinated reactants makes solid-state luminescent measurements a key characterization of the purity of our samples. It can be efficiently combined with PXRD, IR and SQUID measurements to evidence traces of impurities.

All samples have been investigated with fixed fluorimeter experimental conditions to allow easy comparison (see experimental procedures). Figure 9 shows a comparison between S, L, T and US2 that is the most optimized sample from the crystal growth point of view. On all samples no trace of radical ligand is observed. On sample L, that is the sample that clearly presents impurities on SEM images, strong Tb^{III} emission bands are observed (Figure 9 and Table 2) at 489, 544, 580 and 620 nm that can be attributed to the $^5D_4 \rightarrow {}^7F_6$, $^5D_4 \rightarrow {}^7F_5$, $^5D_4 \rightarrow {}^7F_4$ and $^5D_4 \rightarrow {}^7F_3$ f-f transitions, respectively.[89] On sample S, the Tb^{III} emission is reduced but still observable (5.9 and 4 % of integrated intensity, respectively when compared to L) (Table 2). This shows that the hot-filtering (T = 45°C and T = 56°C, respectively) that is expected to prevent the formation of insoluble $[Tb(hfac)_3{\cdot}2H_2O]$ particles on $[Tb(hfac)_3(NIT\text{-}PhOPh)]_n$ crystallites is not fully efficient. This makes all these samples unsuitable for further surface deposition processes. On the contrary, no trace of Tb^{III} emission is observed on the three ultrasonicated samples (US1, US2 and US3). The peak area of the

Tb^{III} $^5D_4 \rightarrow {}^7F_5$ transition is so low that is it comparable to the background of the sample holder (Table 2). This highlights that sonocrystallization prevents the formation of particles of unreacted [$Tb(hfac)_3 \cdot 2H_2O$]. Even with the widest slit aperture for incident UV-light none of the Tb^{III} emission peaks can be distinguished from the sample holder contribution (quartz cuvette of optical grade). This is in line with the hypothesis of an efficient micromixing of the crystallizing solution triggered by sonication.

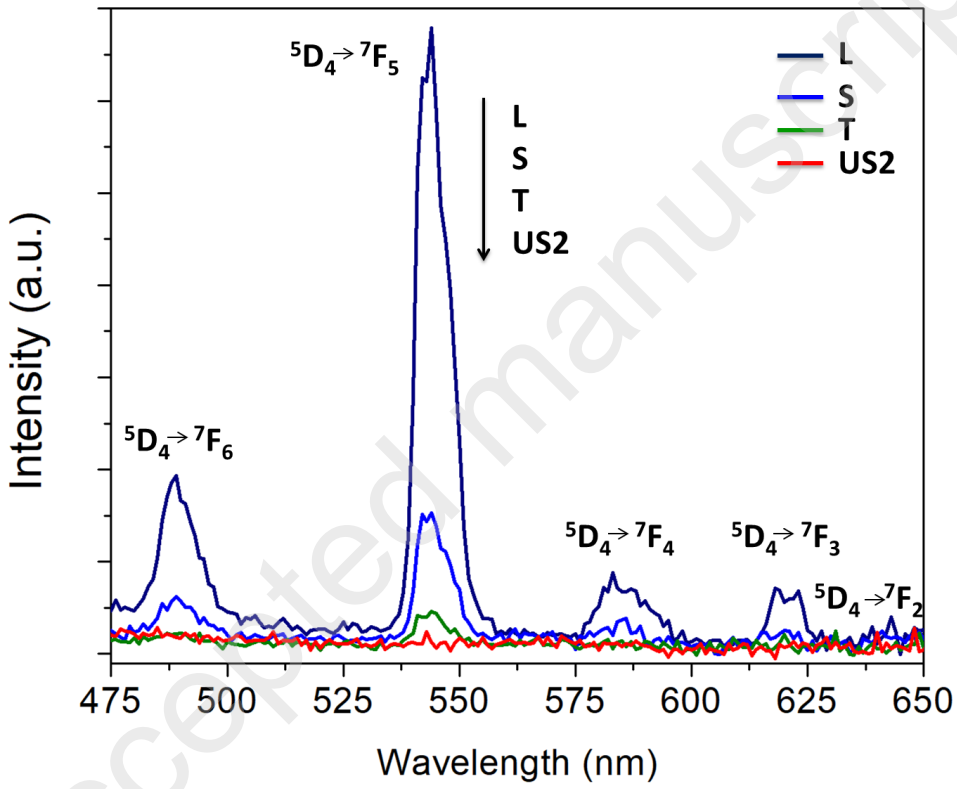

Figure 9. Solid-state luminescence spectra of compounds L, S, T and US2 obtained with λ_{exc} = 312 nm (US1 and US3 are omitted for clarity) at room temperature.

Table 2. Relative Tb^{III} emission measured for the six samples

Sample	Relative peak area of the $^5D_4 \rightarrow {}^7F_5$ transition
Standard (long) crystallization (L)	1
Short crystallization (S)	0.059

Sample	Relative peak area of the $^5D_4 \rightarrow {}^7F_5$ transition
Thermal crystallization (T)	0.040
Ultrasonicated samples (US1, US2, US3)	0.001
Sample holder contribution	0.001

Magnetic Properties

$[Tb(hfac)_3(NIT\text{-}PhOPh)]_n$ has been investigated in the past for its strong Single-Chain Magnet (SCM) properties.[60] This study has been also performed for its Gd, Dy, Ho, Er, Tm and Yb derivatives.[60,93,94] In these reports, samples were made according to a synthetic procedure similar to sample L. In order to check that the SCM property we target is preserved by sonocrystallization, magnetizations versus field curve have been measured at 1.8 K. The very characteristic magnetization shape of $[Tb(hfac)_3(NIT\text{-}PhOPh)]_n$ is observed on all samples (Figure 10). It is composed of an opened hysteresis in zero field with coercive field of ≈ 400 Oe followed by a high-field step (≈ 12500 Oe). The opened hysteresis is due to the efficient magnetic slow relaxation of the chains that are unaffected by quantum tunneling. The high-field step is a consequence of the spin canting with dominant next-nearest-neighbor antiferromagnetic interactions observed in the chains together with a very peculiar crystal packing arrangement.[94] Very little differences can be seen between all curves. This demonstrates that the magnetic behavior of $[Tb(hfac)_3(NIT\text{-}PhOPh)]_n$ is not damaged by the sonication process. However, it can be noted that bulk magnetic measurements are not very sensitive to impurities. This is a severe drawback as far as surface deposition of molecular magnetic compounds is targeted because a control of the magnetic property of a bulk powder is not enough to ensure that the corresponding molecular deposit will be pure and homogenous. Such magnetic impurities could be detrimental for the creation of an effective

magnetic device based on molecular magnetic compounds. This is the reason why magnetic characterizations are not enough to qualify a sample for surface deposition.

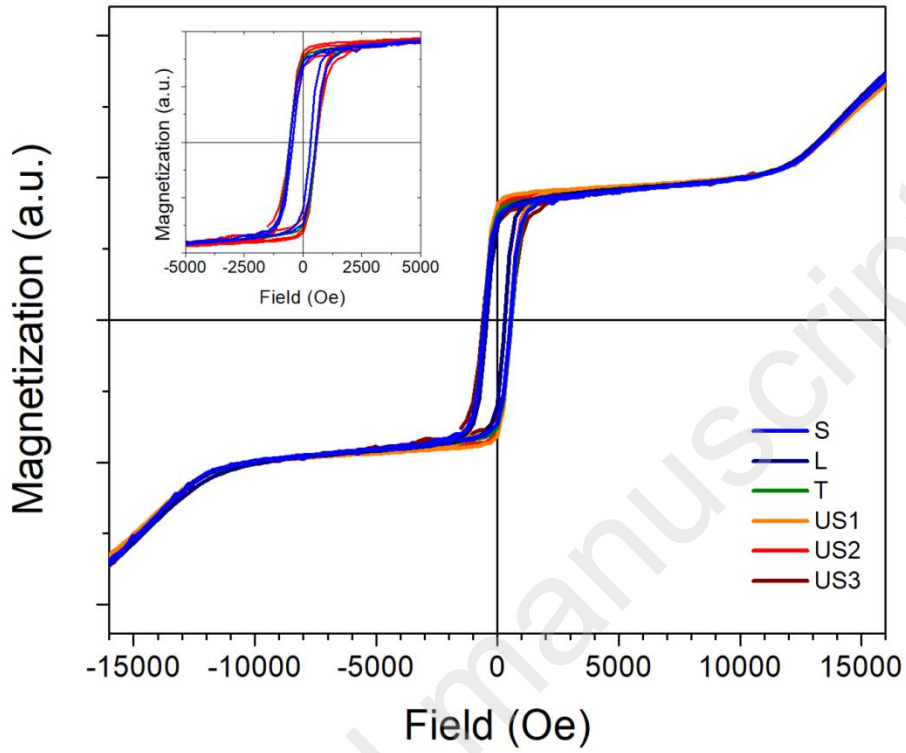

Figure 10. Magnetic hystereses of $[Tb(hfac)_3(NIT\text{-}PhOPh)]_n$ for all samples (S, L, T, US1 – US3). T = 1.8 K, magnetic field sweep rate is 15.5 Oe. s^{-1} (unfitted experimental data)

CONCLUSION

In this study we report a new synthetic pathway for $[Tb(hfac)_3(NIT\text{-}PhOPh)]_n$ using sonocrystallization. The analysis of six different samples shows that this approach allows a size and purity control of the crystallites that is not achievable with conventional crystallization techniques and that is not due to the thermal effect of the sonication. Sonocrystallization impacts the crystallite morphology (rounded apexes, low aspect ratio) when compared to standard crystallization techniques. Additionally, Polydispersity Index in length of the crystallites ($0<PDI_l<1$) is severely reduced from 0.92 on the usual and silent crystallization procedure (L) to 0.16 on the most optimized sonocrystallized sample (US2).

This highlights how sonocrystallization is able to afford highly homogeneous crystallization batches. Interestingly, it can be noted that the PDI optimization is limited to crystallite sizes that are below the dimension of the cavitation bubbles (≈ 10 μm).

For most coordination chemists it is counterintuitive to obtain crystals with a sonication process, because sonication is often mistaken with, or reduced to, sonofragmentation. However, sonication involves a lot of different processes such as sonochemistry,[4,8] sonofragmentation,[6] sonocrystallization[20] and micromixing.[7] In our case, this last mechanism is expected to be the one that allows sonication to produce very pure SCM as demonstrated by solid-state luminescence measurements. Such a high purity upgrade is an asset for the synthesis of pure coordination polymers adapted for further highly sensitive physico-chemical characterizations. Sonocrystallization can be a way to end up with the obsolete sampling of hand-picked crystallites in mother solutions. Our demonstration is based on the use of 24 kHz sonotrodes and it would be interesting to extend it to highest frequencies using transient transducers[95] as well as on different ultrasound reactors.[96]

In conclusion, while sonocrystallization is widely used on purely organic compounds[19,20,22,27,29,97] and on some metal-organic coordination polymers,[35] it seems also very efficient on magnetic coordination compounds. Within some hours it provides samples with optimized crystallite-size distribution, controlled aspect ratio, and significant purity enhancement when compared with conventional silent crystallization techniques. This approach could lead to better sampling of magnetic coordination compounds. This can be particularly useful for characterization or shaping techniques that require pure, morphology- and crystallite-size-controlled bulk samples as in molecular surface science for example.

ACKNOWLEDGEMENTS

This work was supported by INSA Rennes, MIUR-Italy (“Progetto Dipartimenti di Eccellenza 2018-2022” allocated to Department of Chemistry “Ugo Schiff”), CNRS (PICS N°07925 FloRennes) and Region Bretagne (Boost'ERC RECoord N°1122). K.B acknowledges the Institut Universitaire de France (IUF).

Supporting Information Available: sonotrode energy delivery measuremnts and additional thermal profiles. This material is available free of charge via the Internet at http://pubs.acs.org.

Bibliography

(1) Brennen, C. E. *Cavitation and bubble dynamics*; Oxford University Press, 2014.

(2) Wagterveld, R. M.; Boels, L.; Mayer, M. J.; Witkamp, G. J. Visualization of acoustic cavitation effects on suspended calcite crystals. *Ultrason. Sonochem.* **2011**, *18*, 216-225.

(3) Suslick, K. S.; Price, G. J. Applications of ultrasound to materials chemistry. *Annu. Rev. Mater. Sci.* **1999**, *29*, 295-326.

(4) Suslick, K. S. Sonochemistry. *Science* **1990**, *247*, 1439-1445.

(5) Luque de Castro, M. D.; Priego-Capote, F. Ultrasound-assisted crystallization (sonocrystallization). *Ultrason. Sonochem.* **2007**, *14*, 717-724.

(6) Jordens, J.; Appermont, T.; Gielen, B.; Van Gerven, T.; Braeken, L. Sonofragmentation: Effect of Ultrasound Frequency and Power on Particle Breakage. *Cryst. Growth Des.* **2016**, *16*, 6167-6177.

(7) Jordens, J.; Bamps, B.; Gielen, B.; Braeken, L.; Van Gerven, T. The effects of ultrasound on micromixing. *Ultrason. Sonochem.* **2016**, *32*, 68-78.

(8) Suslick, K. S.; Hammerton, D. A.; Cline, R. E. Sonochemical hot spot. *J. Am. Chem. Soc.* **1986**, *108*, 5641-5642.

(9) Kim, H. N.; Suslick, K. S. The Effects of Ultrasound on Crystals: Sonocrystallization and Sonofragmentation. *Crystals* **2018**, *8*, 280.

(10) Pecha, R.; Gompf, B. Microimplosions: Cavitation Collapse and Shock Wave Emission on a Nanosecond Time Scale. *Phys. Rev. Lett.* **2000**, *84*, 1328-1330.

(11) Blake, J. R.; Blake, J. R.; Keen, G. S.; Tong, R. P.; Wilson, M. Acoustic cavitation: the fluid dynamics of non-spherical bubbles. *Phil. Trans. R. Soc. A* **1999**, *357*, 251-267.

(12) Zeiger, B. W.; Suslick, K. S. Sonofragmentation of Molecular Crystals. *J. Am. Chem. Soc.* **2011**, *133*, 14530-14533.

(13) Gao, R.; Gupta, I.; Boyden, E. S. Sonofragmentation of Ultrathin 1D Nanomaterials. *Part. Part. Syst. Charact.* **2017**, *34*, 1600339.

(14) Mandzy, N.; Grulke, E.; Druffel, T. Breakage of TiO2 agglomerates in electrostatically stabilized aqueous dispersions. *Powder Technol.* **2005**, *160*, 121-126.

(15) Suslick, K. S.; Doktycz, S. J. The sonochemistry of zinc powder. *J. Am. Chem. Soc.* **1989**, *111*, 2342-2344.

(16) Doktycz, S.; Suslick, K. Interparticle collisions driven by ultrasound. *Science* **1990**, *247*, 1067-1069.

(17) Richards, W. T.; Loomis, A. L. The chemical effects of high frequency sound waves I. A preliminary survey. *J. Am. Chem. Soc.* **1927**, *49*, 3086-3100.

(18) Vancleef, A.; Seurs, S.; Jordens, J.; Van Gerven, T.; Thomassen, L. C. J.; Braeken, L. Reducing the Induction Time Using Ultrasound and High-Shear Mixing in a Continuous Crystallization Process. *Crystals* **2018**, *8*, 326.

(19) Gielen, B. *Particle engineering by sonocrystallization*; PhD thesis, KU Leuven, Groep Wetenschap & Technologie, 2017.

(20) Jordens, J.; Gielen, B.; Xiouras, C.; Hussain, M. N.; Stefanidis, G. D.; Thomassen, L. C. J.; Braeken, L.; Van Gerven, T. Sonocrystallisation: Observations, theories and guidelines. *Chem. Eng. Process.* **2019**, *139*, 130-154.

(21) Sander, J. R. G.; Zeiger, B. W.; Suslick, K. S. Sonocrystallization and sonofragmentation. *Ultrason. Sonochem.* **2014**, *21*, 1908-1915.

(22) Ruecroft, G.; Hipkiss, D.; Ly, T.; Maxted, N.; Cains, P. W. Sonocrystallization: The Use of Ultrasound for Improved Industrial Crystallization. *Org. Process Res. Dev.* **2005**, *9*, 923-932.

(23) Castillo-Peinado, L. d. l. S.; Luque de Castro, M. D. The role of ultrasound in pharmaceutical production: sonocrystallization. *J. Pharm. Pharmacol.* **2016**, *68*, 1249-1267.

(24) Eder, R. J. P.; Schrank, S.; Besenhard, M. O.; Roblegg, E.; Gruber-Woelfler, H.; Khinast, J. G. Continuous Sonocrystallization of Acetylsalicylic Acid (ASA): Control of Crystal Size. *Cryst. Growth Des.* **2012**, *12*, 4733-4738.

(25) Jordens, J.; Gielen, B.; Braeken, L.; Van Gerven, T. Determination of the effect of the ultrasonic frequency on the cooling crystallization of paracetamol. *Chem. Eng. Process.* **2014**, *84*, 38-44.

(26) Bučar, D.-K.; Elliott, J. A.; Eddleston, M. D.; Cockcroft, J. K.; Jones, W. Sonocrystallization Yields Monoclinic Paracetamol with Significantly Improved Compaction Behavior. *Angew. Chem.-Int. Ed.* **2015**, *54*, 249-253.

(27) Gielen, B.; Kusters, P.; Jordens, J.; Thomassen, L. C. J.; Van Gerven, T.; Braeken, L. Energy efficient crystallization of paracetamol using pulsed ultrasound. *Chem. Eng. Process.* **2017**, *114*, 55-66.

(28) Gogate, P. R.; Pandit, A. B. In *Ultrasound Technologies for Food and Bioprocessing*; Feng, H., Barbosa-Canovas, G., Weiss, J., Eds.; Springer New York: New York, NY, 2011, p 467-493.

(29) Feng, H.; Barbosa-Canovas, G.; Weiss, J.; (Eds) *Ultrasound Technologies for Food and Bioprocessing*, 2011.

(30) Jordens, J.; Canini, E.; Gielen, B.; Van Gerven, T.; Braeken, L. Ultrasound Assisted Particle Size Control by Continuous Seed Generation and Batch Growth. *Crystals* **2017**, *7*, 195.

(31) Dennehy, R. D. Particle Engineering Using Power Ultrasound1. *Org. Process Res. Dev.* **2003**, *7*, 1002-1006.

(32) Lee, J.; Ashokkumar, M.; Kentish, S. E. Influence of mixing and ultrasound frequency on antisolvent crystallisation of sodium chloride. *Ultrason. Sonochem.* **2014**, *21*, 60-68.

(33) Dincer, T. D.; Zisu, B. In *Handbook of Ultrasonics and Sonochemistry*; Ashokkumar, M., Ed.; Springer Singapore: Singapore, 2016, p 1-32.

(34) Taherzade, D.; Soleimannejad, J. Application of ultrasound to the synthesis of a new nanostructured Mn(II) supramolecular compound: A precursor for γ-Mn2O3 nanoparticles. *Ultrason. Sonochem.* **2016**, *32*, 277-283.

(35) Safarifard, V.; Morsali, A. Applications of ultrasound to the synthesis of nanoscale metal–organic coordination polymers. *Coord. Chem. Rev.* **2015**, *292*, 1-14.

(36) Chen, C.-T.; Suslick, K. S. One-dimensional coordination polymers: Applications to material science. *Coord. Chem. Rev.* **1993**, *128*, 293-322.

(37) Kitagawa, S.; Matsuda, R. Chemistry of coordination space of porous coordination polymers. *Coord. Chem. Rev.* **2007**, *251*, 2490-2509.

(38) Zhang, W.-X.; Liao, P.-Q.; Lin, R.-B.; Wei, Y.-S.; Zeng, M.-H.; Chen, X.-M. Metal cluster-based functional porous coordination polymers. *Coord. Chem. Rev.* **2015**, *293-294*, 263-278.

(39) Sessoli, R.; Bernot, K. In *Lanthanides and Actinides in Molecular Magnetism*; Wiley-VCH Verlag GmbH & Co. KGaA: 2015, p 89-124.

(40) Bernot, K. *(Ed.) Molecular Magnetism of Lanthanides Complexes and Networks*; MDPI, 2018

(41) Lorusso, G.; Sharples, J. W.; Palacios, E.; Roubeau, O.; Brechin, E. K.; Sessoli, R.; Rossin, A.; Tuna, F.; McInnes, E. J. L.; Collison, D.; Evangelisti, M. A Dense Metal–Organic Framework for Enhanced Magnetic Refrigeration. *Adv. Mater.* **2013**, *25*, 4653–4656.

(42) Maspoch, D.; Ruiz-Molina, D.; Wurst, K.; Domingo, N.; Cavallini, M.; Biscarini, F.; Tejada, J.; Rovira, C.; Veciana, J. A nanoporous molecular magnet with reversible solvent-induced mechanical and magnetic properties. *Nat Mater* **2003**, *2*, 190-195.

(43) Clérac, R.; Miyasaka, H.; Yamashita, M.; Coulon, C. Evidence for single-chain magnet behavior in a Mn-III-Ni-II chain designed with high spin magnetic units: A route to high temperature metastable magnets. *J. Am. Chem. Soc.* **2002**, *124*, 12837-12844.

(44) Caneschi, A.; Gatteschi, D.; Lalioti, N.; Sangregorio, C.; Sessoli, R.; Venturi, G.; Vindigni, A.; Rettori, A.; Pini, M. G.; Novak, M. A. Cobalt(II)-Nitronyl Nitroxide Chains as Molecular Magnetic Nanowires. *Angew. Chem.-Int. Ed.* **2001**, *40*, 1760-1763.

(45) Shi, W.; Liu, X.; Feng, X.; Meihaus, K. R.; Meng, X.; Zhang, Y.; Li, L.; Liu, J.-L.; Zhang, Y.-Q.; Cheng, P.; Long, J. R. Coercive Fields Above 6 T in Two Cobalt(II)-Radical Chain Compounds. *Angew. Chem.-Int. Ed., n/a*.

(46) Coulon, C.; Miyasaka, H.; Clérac, R. In *Single-Molecule Magnets and Related Phenomena*; Winpenny, R., Ed.; Springer Berlin Heidelberg: 2006; Vol. 122, p 163-206.

(47) Bhowmick, I.; Hillard, E. A.; Dechambenoit, P.; Coulon, C.; Harris, T. D.; Clerac, R. A canted antiferromagnetic ordered phase of cyanido-bridged MnIII2ReIV single-chain magnets. *Chem. Commun.* **2012**, *48*, 9717-9719.

(48) Cassaro, R. A. A.; Reis, S. G.; Araujo, T. S.; Lahti, P. M.; Novak, M. A.; Vaz, M. G. F. A Single-Chain Magnet with a Very High Blocking Temperature and a Strong Coercive Field. *Inorg. Chem.* **2015**, *54*, 9381-9383.

(49) Singh, S. K.; Vignesh, K. R.; Archana, V.; Rajaraman, G. Theoretical insights into the origin of magnetic exchange and magnetic anisotropy in {ReIV-MII} (M = Mn, Fe, Co, Ni and Cu) single chain magnets. *Dalton Trans.* **2016**, *45*, 8201-8214.

(50) Drahoš, B.; Herchel, R.; Trávníček, Z. Single-Chain Magnet Based on 1D Polymeric Azido-Bridged Seven-Coordinate Fe(II) Complex with a Pyridine-Based Macrocyclic Ligand. *Inorg. Chem.* **2018**, *57*, 12718-12726.

(51) Jiang, W.; Jiao, C.; Meng, Y.; Zhao, L.; Liu, Q.; Liu, T. Switching single chain magnet behavior via photoinduced bidirectional metal-to-metal charge transfer. *Chem. Sci.* **2018**, *9*, 617-622.

(52) Liu, X.; Zhang, Y.; Shi, W.; Cheng, P. Rational Design and Synthesis of a Chiral Lanthanide-Radical Single-Chain Magnet. *Inorg. Chem.* **2018**, *57*, 13409-13414.

(53) Pichon, C.; Suaud, N.; Duhayon, C.; Guihéry, N.; Sutter, J.-P. Cyano-Bridged Fe(II)–Cr(III) Single-Chain Magnet Based on Pentagonal Bipyramid Units: On the Added Value of Aligned Axial Anisotropy. *J. Am. Chem. Soc.* **2018**, *140*, 7698-7704.

(54) Liu, X.; Wang, Y.-X.; Han, Z.; Han, T.; Shi, W.; Cheng, P. Tuning the magnetization dynamics of TbIII-based single-chain magnets through substitution on the nitronyl nitroxide radical. *Dalton Trans.* **2019**, *48*, 8989-8994.

(55) Xie, J.; Li, H.-D.; Yang, M.; Sun, J.; Li, L.-C.; Sutter, J.-P. Improved single-chain-magnet behavior in a biradical-based nitronyl nitroxide-Cu–Dy chain. *Chem. Commun.* **2019**, *55*, 3398-3401

(56) Zhao, F.; Dong, Z.-P.; Liu, Z.-L.; Wang, Y.-Q. An unusual homospin CoII ferrimagnetic single-chain magnet with large hysteresis. *CrystEngComm* **2019**, *21*, 6958-6963.

(57) Rams, M.; Jochim, A.; Böhme, M.; Lohmiller, T.; Ceglarska, M.; Rams, M. M.; Schnegg, A.; Plass, W.; Näther, C. Single-Chain Magnet Based on Cobalt(II) Thiocyanate as XXZ Spin Chain. *Chem. Eur. J.* **2020**, *26*, 2837. .

(58) Shi, L.; Shao, D.; Wei, X.-Q.; Dunbar, K.; Wang, X. Enhanced single-chain magnet behavior via anisotropic exchange in a cyano-bridged Mo(III)-Mn(II) chain. *Angew. Chem.-Int. Ed.* **2020**, doi: 10.1002/anie.202001706.

(59) Sun, J.; Xie, J.; Li, L.; Sutter, J.-P. Single-chain magnet behavior in a 2p–3d–4f spin array with a nitronyl nitroxide biradical. *Inorg. Chem. Front.* **2020**, *7*, 1949-1956

(60) Bernot, K.; Bogani, L.; Caneschi, A.; Gatteschi, D.; Sessoli, R. A Family of Rare-Earth-Based Single Chain Magnets:Playing with Anisotropy. *J. Am. Chem. Soc.* **2006**, *128*, 7947-7956.

(61) Benelli, C.; Gatteschi, D. *Introduction to Molecular Magnetism: From Transition Metals to Lanthanides*; Wiley-VCH, Weinheim 2015.

(62) Mas-Balleste, R.; Gomez-Herrero, J.; Zamora, F. One-dimensional coordination polymers on surfaces: towards single molecule devices. *Chem. Soc. Rev.* **2010**, *39*, 4220-4233.

(63) Cornia, A.; Mannini, M.; Sainctavit, P.; Sessoli, R. Chemical strategies and characterization tools for the organization of single molecule magnets on surfaces. *Chem. Soc. Rev.* **2011**, *40*, 3076-3091.

(64) Holmberg, R. J.; Murugesu, M. Adhering magnetic molecules to surfaces. *J. Mater. Chem. C* **2015**, *3*, 11986-11998.

(65) Bogani, L.; Sangregorio, C.; Sessoli, R.; Gatteschi, D. Molecular engineering for single-chain-magnet behavior in a one-dimensional dysprosium-nitronyl nitroxide compound. *Angew. Chem.-Int. Edit.* **2005**, *44*, 5817-5821.

(66) Nečas, D.; Klapetek, P. Gwyddion: an open-source software for SPM data analysis. **2012**, *10*, 181.

(67) Stepto, R. Dispersity in polymer science (IUPAC Recommendations 2009). *Pure Appl. Chem.* **2009**, *81*, 351-353.

(68) Danaei, M.; Dehghankhold, M.; Ataei, S.; Hasanzadeh Davarani, F.; Javanmard, R.; Dokhani, A.; Khorasani, S.; Mozafari, M. R. Impact of Particle Size and Polydispersity Index on the Clinical Applications of Lipidic Nanocarrier Systems. *Pharmaceutics* **2018**, *10*, 57.

(69) Stetefeld, J.; McKenna, S. A.; Patel, T. R. Dynamic light scattering: a practical guide and applications in biomedical sciences. *Biophys. Rev.* **2016**, *8*, 409-427.

(70) Worldwide, M. I. Dynamic Light Scattering, Common Terms Defined. *Inform White Paper; Malvern Instruments Limited: Malvern, UK*, **2011**, 1-6.

(71) Chen, M.; Liu, X.; Fahr, A. Skin penetration and deposition of carboxyfluorescein and temoporfin from different lipid vesicular systems: In vitro study with finite and infinite dosage application. *Int. J. Pharm.* **2011**, *408*, 223-234.

(72) Bain, G. A.; Berry, J. F. Diamagnetic Corrections and Pascal's Constants. *J. Chem. Educ.* **2008**, *85*, 532.

(73) Luther, S.; Mettin, R.; Koch, P.; Lauterborn, W. Observation of acoustic cavitation bubbles at 2250 frames per second. *Ultrason. Sonochem.* **2001**, *8*, 159-162.

(74) Kim, H. N.; Suslick, K. S. Sonofragmentation of Ionic Crystals. *Chem. Eur. J.* **2017**, *23*, 2778-2782.

(75) Guo, Z.; Zhang, M.; Li, H.; Wang, J.; Kougoulos, E. Effect of ultrasound on anti-solvent crystallization process. *J. Cryst. Growth* **2005**, *273*, 555-563.

(76) Li, H.; Wang, J.; Bao, Y.; Guo, Z.; Zhang, M. Rapid sonocrystallization in the salting-out process. *J. Cryst. Growth* **2003**, *247*, 192-198.

(77) Belkacem, N.; Sheikh Salem, M. A.; AlKhatib, H. S. Effect of ultrasound on the physico-chemical properties of poorly soluble drugs: Antisolvent sonocrystallization of ketoprofen. *Powder Technol.* **2015**, *285*, 16-24.

(78) Kordylla, A.; Koch, S.; Tumakaka, F.; Schembecker, G. Towards an optimized crystallization with ultrasound: Effect of solvent properties and ultrasonic process parameters. *J. Cryst. Growth* **2008**, *310*, 4177-4184.

(79) Nii, S.; Takayanagi, S. Growth and size control in anti-solvent crystallization of glycine with high frequency ultrasound. *Ultrason. Sonochem.* **2014**, *21*, 1182-1186.

(80) Kusters, K. A.; Pratsinis, S. E.; Thoma, S. G.; Smith, D. M. Ultrasonic fragmentation of agglomerate powders. *Chem. Eng. Sci.* **1993**, *48*, 4119-4127.

(81) Guo, Z.; Jones, A. G.; Hao, H.; Patel, B.; Li, N. Effect of ultrasound on the heterogeneous nucleation of BaSO4 during reactive crystallization. *J. Appl. Phys.* **2007**, *101*, 054907.

(82) Chow, R.; Blindt, R.; Chivers, R.; Povey, M. A study on the primary and secondary nucleation of ice by power ultrasound. *Ultrasonics* **2005**, *43*, 227-230.

(83) Chow, R.; Blindt, R.; Chivers, R.; Povey, M. The sonocrystallisation of ice in sucrose solutions: primary and secondary nucleation. *Ultrasonics* **2003**, *41*, 595-604.

(84) Ramisetty, K. A.; Pandit, A. B.; Gogate, P. R. Ultrasound-Assisted Antisolvent Crystallization of Benzoic Acid: Effect of Process Variables Supported by Theoretical Simulations. *Industrial & Engineering Chemistry Research* **2013**, *52*, 17573-17582.

(85) Jung, J.; Puget, M.; Cador, O.; Bernot, K.; Calzado, C. J.; Le Guennic, B. Analysis of the Magnetic Exchange Interactions in Yttrium(III) Complexes Containing Nitronyl Nitroxide Radicals. *Inorg. Chem.* **2017**, *56*, 6788-6801.

(86) Gabbaï, F. P.; Chirik, P. J.; Fogg, D. E.; Meyer, K.; Mindiola, D. J.; Schafer, L. L.; You, S.-L. An Editorial About Elemental Analysis. *Organometallics* **2016**, *35*, 3255-3256.

(87) Houard, F.; Evrard, Q.; Calvez, G.; Suffren, Y.; Daiguebonne, C.; Guillou, O.; Gendron, F.; Le Guennic, B.; Guizouarn, T.; Dorcet, V.; Mannini, M.; Bernot, K. Chiral Supramolecular Nanotubes of Single-Chain Magnets. *Angew. Chem.-Int. Ed.* **2020**, *59*, 780-784.

(88) Evrard, Q.; Cucinotta, G.; Houard, F.; Calvez, G.; Suffren, Y.; Daiguebonne, C.; Guillou, O.; Caneschi, A.; Mannini, M.; Bernot, K. Self-assembly of a terbium(III) 1D coordination polymer on mica. *Beilstein J. Nanotechnol.* **2019**, *10*, 2440-2448.

(89) Carnall, W. T.; Fields, P. R.; Rajnak, K. Electronic Energy Levels of the Trivalent Lanthanide Aquo Ions. III. Tb3+. *J. Chem. Phys.* **1968**, *49*, 4447-4449.

(90) Binnemans, K. In *Handbook on the Physics and Chemistry of Rare-Earths*; K.A. Gschneider, J., Bünzli, J. C. G., Pecharsky, V. K., Eds.; Elsevier B.V.: Amsterdam, 2005; Vol. 35.

(91) Beaulac, R.; Bussiere, G.; Reber, C.; Lescop, C.; Luneau, D. Solid-state absorption and luminescence spectroscopy of nitronyl nitroxide radicals. *New J. Chem.* **2003**, *27*, 1200-1206.

(92) Lannes, A.; Intissar, M.; Suffren, Y.; Reber, C.; Luneau, D. Terbium(III) and Yttrium(III) Complexes with Pyridine-Substituted Nitronyl Nitroxide Radical and Different β-Diketonate Ligands. Crystal Structures and Magnetic and Luminescence Properties. *Inorg. Chem.* **2014**, *53*, 9548-9560.

(93) Bernot, K.; Bogani, L.; Sessoli, R.; Gatteschi, D. Tm-III(hfac)(3)(NITPhOPh) (infinity): A new member of a lanthanide-based single chain magnets family. *Inorg. Chim. Acta* **2007**, *360*, 3807-3812.

(94) Bernot, K.; Luzon, J.; Caneschi, A.; Gatteschi, D.; Sessoli, R.; Bogani, L.; Vindigni, A.; Rettori, A.; Pini, M. G. Spin canting in a Dy-based single-chain magnet with dominant next-nearest-neighbor antiferromagnetic interactions. *Phys. Rev. B* **2009**, *79*, 134419.

(95) Keil, F. J.; (Ed.) *Modeling of Process Intensification*, 2007.

(96) Horst, C.; Gogate, P. R.; Pandit, A. B. In *Modeling of Process Intensification* 2007, p 193-277.

(97) Xi, Y.; Li, D. S.; Newbloom, G. M.; Tatum, W. K.; O'Donnell, M.; Luscombe, C. K.; Pozzo, L. D. Sonocrystallization of conjugated polymers with ultrasound fields. *Soft Matter* **2018**, *14*, 4963-4976.